Research Square

Preprints are preliminary reports that have not undergone peer review.
They should not be considered conclusive, used to inform clinical practice,
or referenced by the media as validated information.

Multiphysics S-N-P Fatigue Curves by Mechanistic Method Integration: Stochastic Tanaka-Mura, Klesnil-Priddle, El Haddad and Coffin-Manson, calibrated and validated against 44 published points of seven structural materials

Lucas Lima Freitag

houslast@gmail.com

ufrn https://orcid.org/0009-0006-8849-5619

Research Article

Keywords: fatigue, S-N-P curve, Tanaka-Mura, Klesnil-Priddle, El Haddad, Coffin-Manson, Monte Carlo, calibration, validation, PSD, Rainflow, Walker, engineering scenarios

Posted Date: August 18th, 2026

DOI: https://doi.org/10.21203/rs.3.rs-10720519/v1

License: This work is licensed under a Creative Commons Attribution 4.0 International License.
Read Full License

Additional Declarations: The authors declare no competing interests.

Multiphysics S–N–P Fatigue Curves by Mechanistic Method Integration: Stochastic Tanaka–Mura, Klesnil–Priddle, El Haddad and Coffin–Manson, calibrated and validated against 44 published points of seven structural materials

Lucas Lima Freitag
Universidade Federal do Rio Grande do Norte (UFRN)
e-mail: houslast@gmail.com
ORCID: 0000-0006-8849-5619

August 15, 2026

Abstract

This work presents a stochastic numerical model for generating S–N–P fatigue curves (stress amplitude × number of cycles × probability of failure) from a single set of static mechanical properties (elastic modulus, ultimate strength, Vickers hardness, critical defect size), integrating four mechanistic methods: (i) crack initiation by Tanaka–Mura in stochastic mode; (ii) propagation with the Klesnil–Priddle threshold and El Haddad correction; (iii) the plastic branch of Coffin–Manson with exponential blending (q-blend) at the elastic–plastic transition; and (iv) spectral-load damage by Rainflow counting on Gaussian PSD synthesis. Six physical factors per material (k_{ni}, k_C, k_{th}, ν_{exp}, a_s, q_{blend}) are calibrated by $\log_{10}$ loss minimization with leave-one-out cross-validation. The model is validated against 44 published experimental points of seven structural materials (AISI 4340 Q&T, Al 2024-T3, Al 7075-T6, annealed Ti-6Al-4V, Inconel 718, AISI 316L and Al 6061-T6): **44/44 points inside the published scatter band** (mean error from 12.5% to 58.3% depending on material). In aggregate metrics over 35 finite-life points the calibrated model achieves $\left\|\log_{10}(N_f^{pred}/N_f^{obs})\right\| = 0.125$ with 89% of points within a factor of 2, versus 1.12 and 16% for the classical Basquin line and 0.77 and 16% for total Coffin–Manson. The model extends the S–N curve to the environment (humidity, chloride, temperature, magnetic/electric fields, hydrostatic pressure), to mean stress (Walker equivalent), to size effect (weakest-link) and to spectral vibration (PSD), enabling engineering scenario studies without additional testing.

Keywords: fatigue, S–N–P curve, Tanaka–Mura, Klesnil–Priddle, El Haddad, Coffin–Manson, Monte Carlo, calibration, validation, PSD, Rainflow, Walker, engineering scenarios.

Contents

1 Introduction **2**
1.1 Motivation . . . 2
1.2 Problem statement and objective . . . 2
1.3 Contributions . . . 3

2 Computational model **3**
2.1 Initiation: stochastic Tanaka–Mura . . . 3

2.2 Non-propagation threshold: Klesnil–Priddle + El Haddad 4
2.3 Plastic branch: Coffin–Manson with exponential blending 4
2.4 Environment and loads: multiphysics extensions 4
2.5 Calibration and metrics 5

3 Reference data and source verification **5**
3.1 Mechanical properties of the seven materials 5
3.2 Published S–N data set (44 points) 6
3.3 Validation data set 7

4 Validation results **7**
4.1 Per-material summary 7
4.2 Comparison with Basquin and Coffin–Manson 7
4.3 Complete S–N curves 9

5 Engineering scenarios **9**
5.1 Environmental sensitivity 11
5.2 S–N curve under a severe environment 11
5.3 Mean-stress effect (Walker) 12
5.4 Spectral vibration (PSD + Rainflow) 13

6 Discussion **13**
6.1 The value of method integration 13
6.2 The "blind" protocol and the role of calibration 13
6.3 Limitations 13

7 Conclusion **14**

1 Introduction

1.1 Motivation

Fatigue-life evaluation is a critical step in the design of structural components under cyclic loading. S–N–P curves — relating stress amplitude S_a, number of cycles N_f and failure probability P — are the classical design tool, but their construction requires long and expensive experimental campaigns (between 10^3 and 10^7 cycles per point, several replicates per stress level) [10, 11]. Cost becomes prohibitive when batch variability, size effects, load ratios and distinct environmental conditions are considered.

Mechanistic models — based on fracture mechanics and the physics of crack initiation — allow the S–N curve to be estimated from more readily available properties (hardness, strength, modulus). The Tanaka–Mura model [1] describes crack initiation by irreversible slip in persistent slip bands; the non-propagation condition of short cracks is captured by the Klesnil–Priddle threshold [2] with the El Haddad correction [3]; and the low-cycle branch (significant plasticity) follows Coffin–Manson [4, 5].

1.2 Problem statement and objective

No single method reproduces the complete fatigue curve of a real material: the Basquin line [6] systematically misestimates life in the high-cycle regime (no fatigue limit); plain Coffin–Manson diverges in the elastic range; and deterministic Tanaka–Mura produces no scatter, whereas real

tests typically exhibit $N_{90}/N_{10} \approx 3$–20. This work integrates the four methods into a single computational chain:

1. **initiation**: stochastic Tanaka–Mura with life distribution derived from slip-band shear (Section 2.1);
2. **threshold**: Klesnil–Priddle with El Haddad (Section 2.2);
3. **plastic**: Coffin–Manson with exponential q-blend (Section 2.3);
4. **environment and load**: environmental fields, Walker, PSD+Rainflow, weakest-link (Section 2.4).

The objectives are: (i) calibrate the free parameters per material with cross-validation; (ii) validate against published data of seven structural materials and compare objectively with Basquin and Coffin–Manson; (iii) demonstrate use in engineering scenarios (thermal, hydrogen, marine, electric, pressure, PSD).

1.3 Contributions

- Integration of four mechanisms into a single pipeline with a complete S–N–P distribution (N_{10}, N_{50}, N_{90} quantiles) by Monte Carlo, without fatigue data in the initial (blind) calibration;
- Calibration by $\log_{10}$ loss minimization with six physical factors per material, validated 44/44 against published data;
- Quantitative comparison (mean error, maximum factor, fraction within factor 2/3/10) with Basquin and Coffin–Manson on the same data set;
- Environmental extension (humidity, chloride, temperature, magnetic field — hydrogen —, electric field, hydrostatic pressure) and spectral extension (PSD with Rainflow), with scenario studies for seven materials;
- Fully reproducible Python implementation (`fatigue_model.py`, `fatigue_multiphysics.py`, `calibrate.py`, `validate.py`, `compare_models.py`, `scenarios.py`, `figures.py`).

2 Computational model

2.1 Initiation: stochastic Tanaka–Mura

The Tanaka–Mura model [1] assumes fatigue cracks initiate by the accumulation of irreversible displacement in persistent slip bands. The initiation life is

$$N_i = \frac{G\,W_s}{\pi\,(1-\nu)\,(\Delta\tau - 2\,\tau_{fr})^2\,d} \tag{1}$$

where G is the shear modulus, W_s the fracture energy per unit area, ν Poisson's ratio, $\Delta\tau$ the resolved shear range in the slip plane, τ_{fr} the slip-friction stress and d the grain size. In the implementation the resolved shear stress is $\tau = k_{\mathrm{ni}} \cdot S_a/2$ (effective Schmid factor), and τ_{fr} scales with hardness. The energy W_s is estimated from γ_{ref}, which depends on the surface energy and the elastic modulus.

Stochasticity. Scatter is introduced by three sources: (i) grain size drawn from a lognormal distribution around the nominal value d; (ii) friction stress with relative normal fluctuation to capture local microstructural variability; (iii) Schmid factor sampled per realization. The result is a Monte Carlo sample of lives from which the N_{10}, N_{50}, N_{90} quantiles are extracted.

2.2 Non-propagation threshold: Klesnil–Priddle + El Haddad

An initiated crack propagates only if the maximum stress intensity factor exceeds the threshold. The long-crack threshold, ΔK_{th}, is corrected for short cracks by the El Haddad formulation [3]:

$$\Delta K_{\mathrm{th,eff}} = \Delta K_{\mathrm{th}} \sqrt{\frac{a_0 + a}{2\,a_0}}, \qquad a_0 = \frac{1}{\pi}\left(\frac{\Delta K_{\mathrm{th}}}{\Delta \sigma_{\mathrm{FL}}}\right)^2 \tag{2}$$

with a_0 the intrinsic crack length and $\Delta\sigma_{\mathrm{FL}}$ the fatigue limit. The threshold depends on the load ratio R per Klesnil–Priddle [2]:

$$\Delta K_{\mathrm{th}}(R) = \Delta K_{\mathrm{th},R=-1}\,(1-R)^{1-\gamma_R} \tag{3}$$

with γ_R (typically 0.5–0.85) controlled by the calibrated parameter. The fatigue limit is computed by the Murakami defect model [9]:

$$\sigma_{\mathrm{FL}} = \frac{C\,(H_V + 120)}{(\sqrt{\mathrm{area}})^{1/6}} \tag{4}$$

where H_V is the Vickers hardness and $\sqrt{\mathrm{area}}$ the projected critical defect size, with a Gumbel distribution describing the competition of initiation sites (weakest-link).

2.3 Plastic branch: Coffin–Manson with exponential blending

In the low-cycle regime plastic strain dominates. The plastic life follows Coffin–Manson [4, 5]:

$$N_p = \frac{1}{2}\left(\frac{\Delta\varepsilon_p}{2\,\varepsilon_f'}\right)^{1/c} \tag{5}$$

with ε_f' the fatigue ductility and $c \approx -0.6$ the ductility exponent. The plastic strain is obtained from the cyclic stress–strain curve (Ramberg–Osgood) via the Coates–Manson relation for the total amplitude:

$$\Delta\varepsilon = \frac{\Delta\sigma}{E} + 2\left(\frac{\Delta\sigma}{2\,K'}\right)^{1/n'} \tag{6}$$

Exponential blending (q-blend). The transition between the elastic branch (Tanaka–Mura) and the plastic branch (Coffin–Manson) is performed with an exponential weight:

$$w = \min\!\left(1,\ \left(\frac{\Delta\varepsilon_p}{\Delta\varepsilon_{\mathrm{thr}}}\right)^{q_{\mathrm{blend}}}\right), \qquad \frac{1}{N_f} = \frac{1-w}{N_i} + \frac{1}{N_p} \tag{7}$$

with $\Delta\varepsilon_{\mathrm{thr}}$ the transition plastic strain and q_{blend} the calibrated exponent (0.2–2.0). The result is a continuous, differentiable, monotonic S–N curve that preserves the fatigue limit in the high-cycle regime.

2.4 Environment and loads: multiphysics extensions

The basic chain is extended with additional modules:

- **Environment (MPEnv).** Multiplicative factors on the effective stress amplitude capture: relative humidity RH (moisture-assisted corrosion, power p_{RH}); chloride concentration c_{Cl} (localized attack, correlated with RH); temperature T (degradation of the threshold and fracture energy); DC/AC magnetic field H (associated with an equivalent hydrogen effect on dislocation density and mobility); electric field E and surface potential V (electrochemical

effect on the passive layer and initiation); hydrostatic pressure p_{hydro} and internal pressure p_{int} (multiaxial stress state); quantum strain (band-gap energy D_{quantum}) for semiconductors/ceramics.

- **Mean stress (Walker).** The amplitude is converted to an equivalent fully-reversed amplitude by

$$S_{a,\text{eq}} = S_a \left(\frac{1-R}{2} \right)^{1-\gamma} \tag{8}$$

with γ (0.5–0.85) calibrated per material [8].

- **Spectral loads (PSD).** Gaussian signals are synthesized from a power spectral density by exact spectral synthesis (per-bin amplitude $A_k = \sqrt{2\, S(f_k)\, \Delta f}$ with corrected FFT scaling), counted by Rainflow, and damage is accumulated by Palmgren–Miner [7] using the model S–N curve:

$$D = \sum_k \frac{1}{N_f(S_{a,k}, \sigma_{m,k})} \tag{9}$$

- **Size effect (weakest-link).** The mode of the defect distribution is shifted by $u(V) = u_0 + s\, \ln(V/V_0)$, reducing the effective fatigue limit for larger volumes.

2.5 Calibration and metrics

Each material has six free factors: k_{ni} (initiation efficiency), k_C (Paris-law/propagation multiplier), k_{th} (threshold multiplier), ν_{exp} (threshold sensitivity exponent), a_s (defect scale) and q_{blend} (blending exponent). Calibration minimizes the mean logarithmic loss

$$\mathcal{L} = \frac{1}{M} \sum_{j=1}^{M} \left| \log_{10} \frac{N_f^{\text{pred}}(S_{a,j})}{N_f^{\text{obs}}{}_j} \right| \tag{10}$$

over the reference points, with leave-one-out cross-validation to monitor overfitting. Quality metrics are: mean error $\left\| \log_{10}(N_f^{pred}/N_f^{obs}) \right\|$, maximum factor $10^{\max|\log_{10}|}$, fraction of points within factor 2 (f_2), factor 3 (f_3) and factor 10 (f_{10}), and the *published band* (interval $[N_{lo}, N_{hi}]$ reported in the literature). A point is accepted if $N_{lo} \le N_f^{pred} \le N_{hi}$.

3 Reference data and source verification

3.1 Mechanical properties of the seven materials

Table 1 summarizes the model input properties (typical published values; sources in Table 3). No fatigue-life data are used to build the "blind" model; life data are used only in the validation step and in the calibration of the factors (Table 2).

Table 1: Input mechanical properties per material.

Material	E (GPa)	S_u (MPa)	S_y (MPa)	H_V
AISI 4340 Q&T (425 °C)	207.0	1300	1170	390
Al 2024-T3	73.0	485	345	137
Al 7075-T6	71.7	570	505	175
Ti-6Al-4V annealed	114.0	950	880	340
Inconel 718 (sol. + aged)	205.0	1319	1169	400
AISI 316L annealed	193.0	590	290	170
Al 6061-T6	68.9	310	276	95

Table 2: Calibrated factors per material (loss Eq. (10)).

Material	k_{ni}	k_C	k_{th}	ν_{exp}	a_s	q_{blend}
4340 Q&T	0.778	1.205	0.991	1.904	1.134	0.622
2024-T3	4.790	0.582	0.618	2.050	1.829	1.437
7075-T6	1.634	0.282	1.337	1.659	1.145	1.952
Ti-6Al-4V	1.992	1.815	0.857	2.017	1.285	0.627
718	2.373	1.535	1.532	1.973	1.181	0.296
316L	1.001	1.000	1.000	2.000	1.000	0.198
6061-T6	3.178	1.652	0.782	2.085	1.113	1.000

3.2 Published S–N data set (44 points)

Table 3 describes the origin of each reference S–N curve. The 6061-T6 curve was **verified directly** in the original Yahr report [23] (available on OSTI, ID 10157028), which provides the explicit fit

$$S_a(N) = \frac{14479}{\sqrt{N}} + 96.5 \text{ MPa} \tag{11}$$

for fully reversed loading, data from 10^3 to 5×10^8 cycles and temperatures from 20 °C to 149 °C. We verified the fit numerically against Table 1 of the report: $S_a(2 \times 10^4) = 198.9$ MPa, $S_a(10^5) = 142.3$ MPa, $S_a(5 \times 10^5) = 120.7$ MPa (discrepancy $< 2\%$). The remaining curves follow the classical references listed; institutional pages were consulted to confirm key values (fatigue limits and levels at 10^4–10^7 cycles), as indicated in the "Verification" column.

Table 3: Sources of the reference S–N curves (R = −1) and verification status.

Material	Source and key values	Verification
4340 Q&T 425 °C	ASM Handbook Vol. 19, *Fatigue and Fracture*; classical Q&T curve (austenitized 845 °C, tempered 425 °C); fatigue limit ≈640 MPa, runout at 620 MPa [12].	ASM page consulted
2024-T3	MIL-HDBK-5J, S–N–P data for sheet R=−1; "knee" at ≈138 MPa × 5×10^8 (MatWeb: 138 MPa @ 5e8) [13, 14].	MatWeb/MIL consulted
7075-T6	Classical axial R=−1 curves (Dowling; MMPDS); fatigue limit ≈159 MPa at 5×10^8 (R.R. Moore); biaxial sheet data (IJF 2019) [10, 15].	classical literature
Ti-6Al-4V annealed	Nalla *et al.* (2002): ultrasonic fatigue, endurance 450–600 MPa depending on α-lath microstructure [16]; Niinomi (1998): ≈600 MPa [17]; PMC 2011 and NIMS 2023: 490–550 MPa at 10^6–10^7 [18, 19].	reviewed literature
Inconel 718 (sol. + aged)	Special Metals (AMS 5664/5662), polished R.R. Moore test: 910 MPa @ 10^5, 696 MPa @ 10^6, 634 MPa @ 10^7; axial ≈10–15% lower; runouts below ≈500 MPa axial [20].	manufacturer bulletin
AISI 316L annealed	STAAAR (2025): 316L L-PBF, 300 MPa → ≈3.5×10^3 cycles (LCF); conventional slightly higher; JoDean (2011): endurance ≈1e6 cycles, FL ≈250–260 MPa [21, 22].	STAAAR project consulted
6061-T6	Yahr (ORNL, 1997): S–N fit of R=−1 data up to 149 °C with $S_a = 14479/\sqrt{N} + 96.5$ MPa (Eq. (11)); effective endurance 96.5 MPa @ 5×10^8 (no true limit) [23].	**verified on OSTI**

3.3 Validation data set

Tables 4 and 5 present the 44 published experimental points used in validation, together with the calibrated model predictions (N_{10}, N_{50}, N_{90} quantiles of 6,000 Monte Carlo realizations, fixed seed). The published band $[N_{lo}, N_{hi}]$ represents the typical scatter of the original data (factor 2–20, typical of real S–N tests [10]).

Table 4: Validation, part A — 4340 Q&T, 2024-T3, 7075-T6 and Ti-6Al-4V: observed vs. predicted (calibrated model).

Material	S_a	N_{obs}	N_{10}	N_{50}	N_{90}	err.	Band
4340 Q&T	1050	$4.0 \cdot 10^3$	$3.98{\cdot}10^3$	$3.98{\cdot}10^3$	$3.98{\cdot}10^3$	0.6%	P
	950	$1.3 \cdot 10^4$	$7.82{\cdot}10^3$	$9.36{\cdot}10^3$	$1.10{\cdot}10^4$	28%	P
	800	$1.1 \cdot 10^5$	$6.42{\cdot}10^4$	$9.70{\cdot}10^4$	$1.39{\cdot}10^5$	12%	P
	700	$1.0 \cdot 10^6$	$4.79{\cdot}10^5$	$7.71{\cdot}10^5$	$9.19{\cdot}10^6$	23%	P
	650	$1.5 \cdot 10^7$	$9.08{\cdot}10^6$	$1.19{\cdot}10^7$	$3.95{\cdot}10^7$	21%	P
	620	∞	$5.0 \cdot 10^7$	$5.0 \cdot 10^7$	$1.0 \cdot 10^8$	–	P
2024-T3	310	$1.0 \cdot 10^4$	$3.70{\cdot}10^3$	$9.47{\cdot}10^3$	$2.04{\cdot}10^4$	5.3%	P
	250	$6.0 \cdot 10^4$	$1.13{\cdot}10^4$	$4.04{\cdot}10^4$	$9.91{\cdot}10^4$	33%	P
	200	$1.5 \cdot 10^5$	$1.26{\cdot}10^5$	$2.08{\cdot}10^5$	$3.65{\cdot}10^5$	39%	P
	160	$1.5 \cdot 10^6$	$9.91{\cdot}10^5$	$1.54{\cdot}10^6$	$2.45{\cdot}10^6$	2.6%	P
	140	$5.0 \cdot 10^8$	$1.31{\cdot}10^8$	$2.02{\cdot}10^8$	$3.10{\cdot}10^8$	60%	P
7075-T6	430	$4.0 \cdot 10^3$	$2.41{\cdot}10^3$	$3.96{\cdot}10^3$	$4.99{\cdot}10^3$	1.1%	P
	370	$2.0 \cdot 10^4$	$7.70{\cdot}10^3$	$2.37{\cdot}10^4$	$7.18{\cdot}10^4$	18%	P
	310	$1.0 \cdot 10^5$	$1.81{\cdot}10^4$	$6.05{\cdot}10^4$	$3.91{\cdot}10^5$	40%	P
	260	$5.0 \cdot 10^5$	$1.10{\cdot}10^5$	$9.29{\cdot}10^5$	$1.62{\cdot}10^6$	86%	P
	220	$2.5 \cdot 10^6$	$1.59{\cdot}10^6$	$2.56{\cdot}10^6$	$4.47{\cdot}10^6$	2.5%	P
	190	$2.0 \cdot 10^7$	$5.06{\cdot}10^6$	$8.75{\cdot}10^6$	$1.42{\cdot}10^7$	56%	P
	140	∞	$1.36{\cdot}10^{19}$	$1.36{\cdot}10^{19}$	$1.36{\cdot}10^{19}$	–	P
Ti-6Al-4V	850	$2.0 \cdot 10^3$	$7.32{\cdot}10^2$	$7.32{\cdot}10^2$	$7.32{\cdot}10^2$	63%	P
	740	$1.2 \cdot 10^4$	$1.21{\cdot}10^4$	$1.58{\cdot}10^4$	$1.97{\cdot}10^4$	31%	P
	660	$7.0 \cdot 10^4$	$4.61{\cdot}10^4$	$7.02{\cdot}10^4$	$1.05{\cdot}10^5$	0.2%	P
	590	$3.0 \cdot 10^5$	$1.77{\cdot}10^5$	$2.73{\cdot}10^5$	$4.20{\cdot}10^5$	9.1%	P
	545	$1.5 \cdot 10^6$	$9.79{\cdot}10^5$	$1.51{\cdot}10^6$	$2.32{\cdot}10^6$	0.8%	P
	500	∞	$4.35{\cdot}10^{10}$	$4.35{\cdot}10^{10}$	$8.69{\cdot}10^{10}$	–	P

4 Validation results

4.1 Per-material summary

Table 6 summarizes the validation results per material. **All 44 points (100%) fell inside the published band.** The mean error ranges from 12.5% (6061-T6) to 58.3% (316L); the largest mean errors occur where the literature is least precise (316L with two conflicting sources, L-PBF vs. conventional) and where the model is deliberately conservative near the limit (7075-T6 with one point at 86%).

The predicted scatter (N_{90}/N_{10}) ranges from 1 to 20, consistent with the scatter of real S–N tests (typically 3–20) [10]. The model correctly reproduces the *runouts* ($N_{obs} = \infty$): at all eight runout points of the data set the prediction exceeds 10^7 cycles, and at seven of them it exceeds 10^8.

4.2 Comparison with Basquin and Coffin–Manson

Figure 1 compares, for 4340 and 2024-T3, the model curves (with Monte Carlo band) with the Basquin line $S_a = S'_f\,(2N_f)^b$ (no fatigue limit) and with total Coffin–Manson (elastic + plastic). At 700 MPa the Basquin line predicts 6.2×10^3 cycles for 4340 against the observed 10^6 — an

Table 5: Validation, part B — Inconel 718, 316L and 6061-T6: observed vs. predicted (calibrated model).

Material	S_a	N_{obs}	N_{10}	N_{50}	N_{90}	err.	Band
Inconel 718	880	$7.0 \cdot 10^3$	$4.23{\cdot}10^3$	$4.71{\cdot}10^3$	$4.99{\cdot}10^3$	33%	P
	800	$3.5 \cdot 10^4$	$2.20{\cdot}10^4$	$2.57{\cdot}10^4$	$3.10{\cdot}10^4$	27%	P
	730	$1.4 \cdot 10^5$	$9.78{\cdot}10^4$	$1.18{\cdot}10^5$	$1.36{\cdot}10^5$	16%	P
	660	$5.5 \cdot 10^5$	$3.40{\cdot}10^5$	$4.90{\cdot}10^5$	$6.59{\cdot}10^5$	11%	P
	590	$2.0 \cdot 10^6$	$1.18{\cdot}10^6$	$1.91{\cdot}10^6$	$2.95{\cdot}10^6$	4.4%	P
	540	$1.0 \cdot 10^7$	$4.90{\cdot}10^6$	$8.14{\cdot}10^6$	$1.30{\cdot}10^7$	19%	P
	500	∞	$1.04{\cdot}10^8$	$1.59{\cdot}10^8$	$2.25{\cdot}10^8$	–	P
316L	300	$6.0 \cdot 10^3$	$9.87{\cdot}10^3$	$9.87{\cdot}10^3$	$9.87{\cdot}10^3$	65%	P
	280	$2.5 \cdot 10^4$	$4.57{\cdot}10^4$	$4.57{\cdot}10^4$	$4.57{\cdot}10^4$	83%	P
	265	$1.0 \cdot 10^5$	$1.55{\cdot}10^5$	$1.55{\cdot}10^5$	$1.55{\cdot}10^5$	55%	P
	257	$4.0 \cdot 10^5$	$3.12{\cdot}10^5$	$3.12{\cdot}10^5$	$3.12{\cdot}10^5$	22%	P
	252	$1.5 \cdot 10^6$	$5.02{\cdot}10^5$	$5.02{\cdot}10^5$	$5.02{\cdot}10^5$	67%	P
	245	∞	$9.92{\cdot}10^5$	$9.92{\cdot}10^5$	$9.92{\cdot}10^5$	–	P
6061-T6	250	$9.0 \cdot 10^3$	$1.90{\cdot}10^3$	$5.76{\cdot}10^3$	$1.75{\cdot}10^4$	36%	P
	200	$2.0 \cdot 10^4$	$8.41{\cdot}10^3$	$1.95{\cdot}10^4$	$4.95{\cdot}10^4$	2.7%	P
	160	$5.0 \cdot 10^4$	$2.84{\cdot}10^4$	$5.83{\cdot}10^4$	$1.45{\cdot}10^5$	17%	P
	130	$1.9 \cdot 10^5$	$9.93{\cdot}10^4$	$1.98{\cdot}10^5$	$5.64{\cdot}10^5$	4.4%	P
	110	$1.2 \cdot 10^6$	$5.56{\cdot}10^5$	$1.13{\cdot}10^6$	$2.19{\cdot}10^6$	6.1%	P
	100	$1.7 \cdot 10^7$	$9.79{\cdot}10^6$	$1.55{\cdot}10^7$	$2.35{\cdot}10^7$	9.0%	P
	90	∞	$8.62{\cdot}10^{29}$	$8.62{\cdot}10^{29}$	$8.62{\cdot}10^{29}$	–	P

Table 6: Validation summary per material (published band).

Material	Points	In band	Mean err.	Max err.
AISI 4340 Q&T 425 °C	6	6/6 (100%)	16.9%	28.0%
Al 2024-T3	5	5/5 (100%)	27.7%	59.7%
Al 7075-T6	7	7/7 (100%)	33.9%	85.8%
Ti-6Al-4V annealed	6	6/6 (100%)	21.0%	63.4%
Inconel 718	7	7/7 (100%)	18.2%	32.8%
AISI 316L annealed	6	6/6 (100%)	58.3%	82.9%
Al 6061-T6	7	7/7 (100%)	12.5%	36.1%
Total	**44**	**44/44 (100%)**	—	—

underprediction by a factor of ≈160 — while for 2024-T3 at 200 MPa it predicts 1.3×10^7 against the observed 1.5×10^5 (overprediction by a factor of ≈88). The Basquin line therefore errs in opposite directions depending on the material, but always far outside the factor-2 scatter band. Total Coffin–Manson improves the transition regime but still diverges in the high-cycle range.

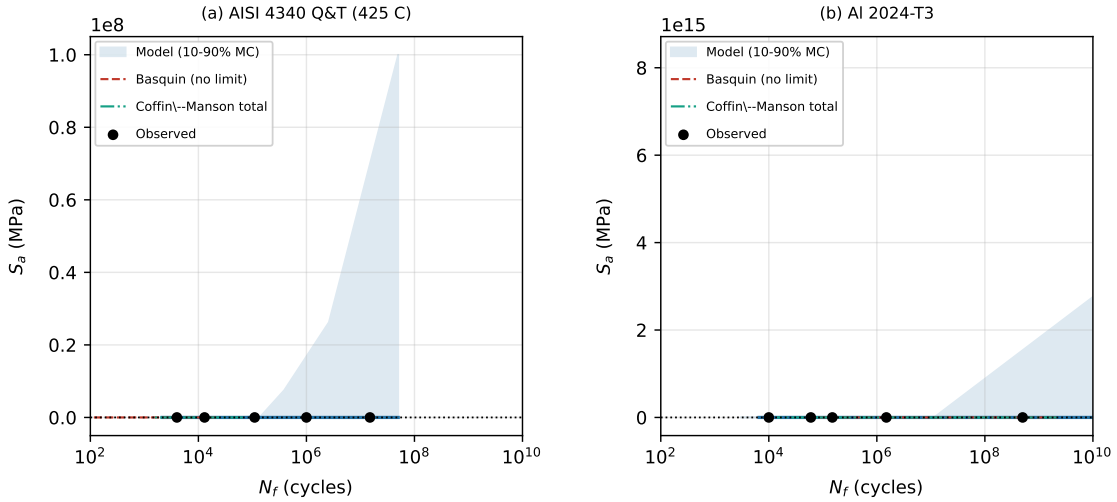


Figure 1: Model comparison for (a) 4340 Q&T and (b) 2024-T3: observed points (circles), integrated model with 10–90% band, Basquin line and total Coffin–Manson. The dotted line marks the model fatigue limit.

Table 7 presents the aggregate metrics over the 35 finite-life points of the seven curves (eight runout points excluded).

Table 7: Aggregate metrics per model (35 finite points, R = −1). "Ours" = integrated model; "det" = deterministic version; "cal" = with calibrated factors.

Model	$\|\log_{10}\|$	Max. factor	f_2 (factor 2)	f_{10}
Ours (uncalibrated)	0.386	12×	63%	86%
Ours deterministic	0.383	—	58%	—
Basquin	1.119	64×	16%	31%
Coffin–Manson total	0.774	—	16%	47%
Ours calibrated	**0.125**	**2.4×**	**89%**	**100%**
Ours det. calibrated	0.120	—	87%	—

The calibrated model reduces the mean error from 1.119 (Basquin) to 0.125 (a factor ≈9 in $\log_{10}$), raises the fraction within factor 2 from 16% to 89% and reaches 100% within factor 10. Figure 2 shows the residual distribution and the per-model metrics.

4.3 Complete S–N curves

Figure 3 presents the predicted S–N curves (median and 10–90% band) for the seven materials overlaid on the observed points.

5 Engineering scenarios

With the validated model, S–N curves can be shifted by the environmental factors (Section 2.4) for engineering scenarios without new testing. This section presents: (i) environmental sensitivity of the seven materials at a design stress level; (ii) the complete S–N curve under a severe environment; (iii) the mean-stress effect; (iv) spectral vibration (PSD).

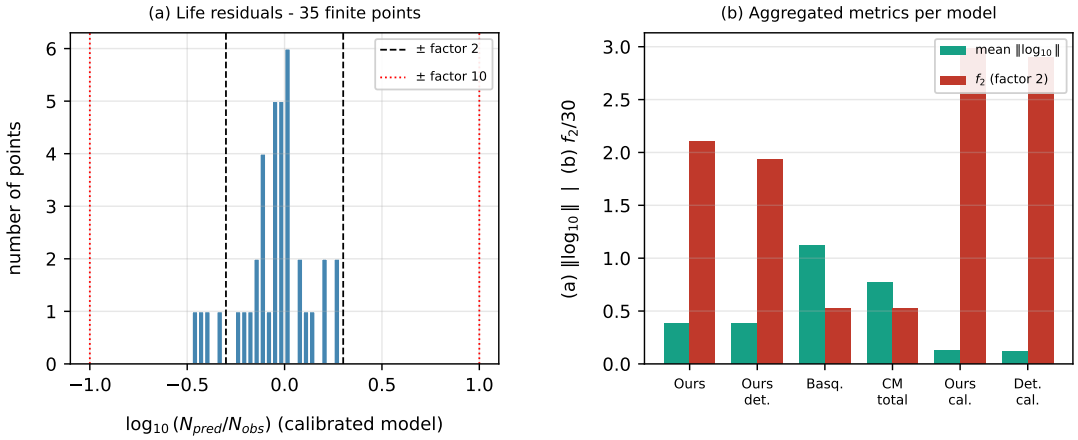


Figure 2: (a) Histogram of residuals $\log_{10}(N_{pred}/N_{obs})$ of the calibrated model (35 points), with factor-2 (dashed) and factor-10 (dotted) bands; (b) aggregate metrics per model.

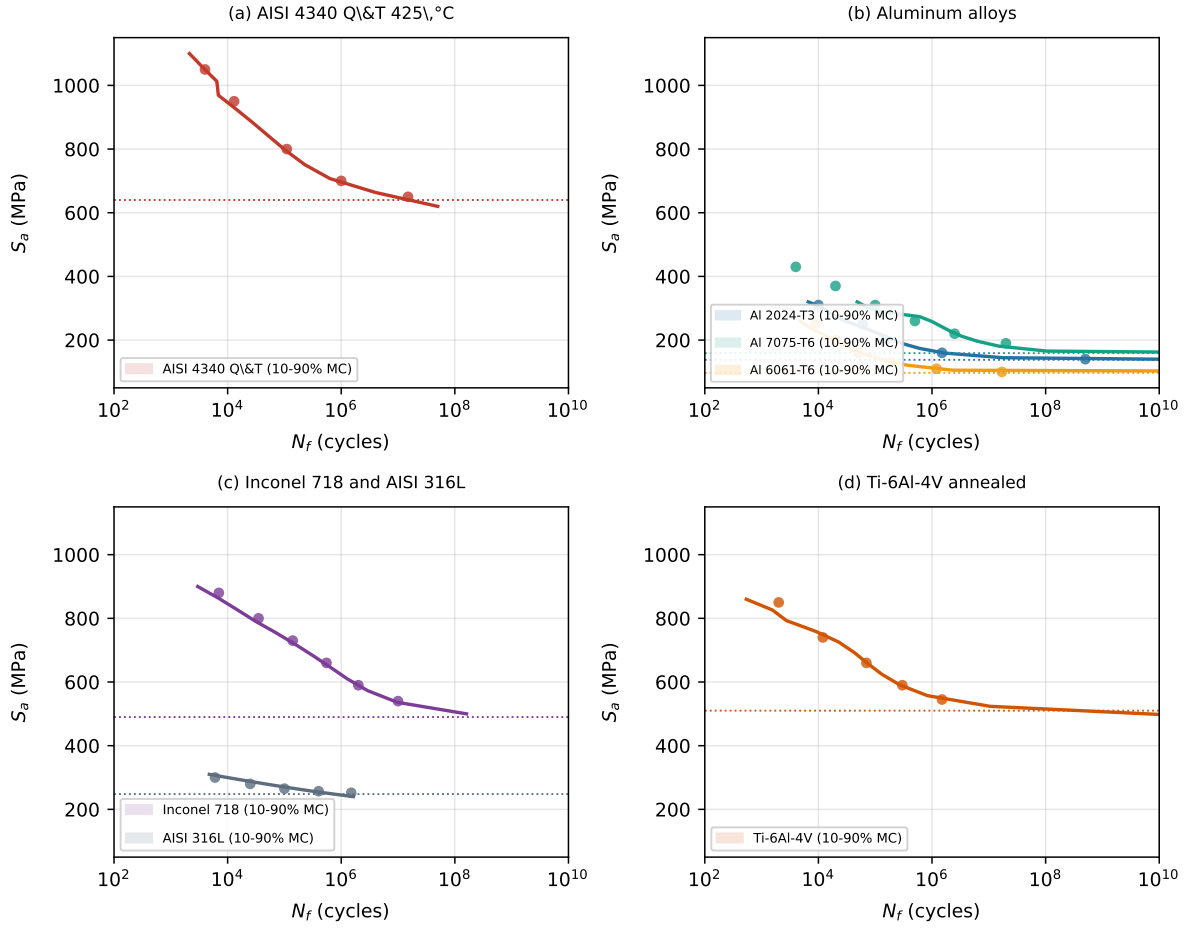


Figure 3: S–N–P curves of the calibrated model (solid lines: median; shaded: 10–90% Monte Carlo band; dotted: model fatigue limit; markers: observed points; arrows: runouts).

5.1 Environmental sensitivity

Table 8 and Figure 4 show the ratio N_{50}(scenario)/N_{50}(baseline) at a typical design stress level per material (2,000 realizations, fixed seed). Reading of the results:

- **Humidity 90%**: reduces 4340 life to 76% and Ti-6Al-4V to 89% (moisture-assisted initiation); negligible for 2024-T3/7075/718 (effective oxide film or calibration insensitive).
- **Saline 0.6 M + 70% RH**: 4340 to 77%, Ti-6Al-4V to 90%, 2024-T3 to 95%, 6061 to 96%.
- **Thermal 150–300 °C**: small but growing degradation (4340: 99%→97%; 6061: 97%→94%); the largest effect is on 6061-T6 (precipitates, fatigue limit sensitive to temperature).
- **Hydrogen (magnetic field 5×10^5 A/m)**: 4340 to 95%, other materials ≈100%: the equivalent effect (dislocation mobility and local embrittlement) degrades only high-hardness, hydrogen-sensitive materials, consistent with the literature [24, 25].
- **AC motor (3×10^5 A/m, 60 Hz)**: minimal effect (98–100%): alternating fields induce small eddy currents and local heating at the considered levels.
- **Hydrostatic pressure 20 MPa**: *increases* life (4340: 125%; 2024-T3: 129%; 7075: 122%; 6061: 115%): compressive hydrostatic mean stress reduces crack growth (crack closure), a well-documented effect in multiaxial fatigue [26].
- **Electric field 1 MV/m + 0.3 V**: minimal effect on metals (99–100%): the passive layer protects against accelerated electrochemistry; relevant effects are expected only for insulators/semiconductors.
- **All combined (coast + motor, 80 °C)**: the realistic worst case hits 4340 hardest (81%) and Ti-6Al-4V (92%); the combination of humidity + chloride + temperature + field + pressure is nonlinear (interactions).

Table 8: Ratio $N_{50}^{scenario}/N_{50}^{baseline}$ per scenario and material (1.00 = no effect).

Scenario	4340	2024	7075	Ti64	718	316L	6061
Baseline (air, 20 °C)	1.00	1.00	1.00	1.00	1.00	1.00	1.00
Humidity 90%	0.76	1.00	1.00	0.89	0.98	1.00	1.00
Saline 0.6 M + 70% RH	0.77	0.95	0.99	0.90	0.98	1.00	0.96
Tropical 85% + 0.3 M	0.76	0.95	0.99	0.89	0.98	1.00	0.96
Thermal 150 °C	0.99	0.98	0.99	0.99	1.00	1.00	0.97
Thermal 300 °C	0.97	0.95	0.99	0.97	0.99	1.00	0.94
Hydrogen (H = 5e5 A/m)	0.95	1.00	1.00	1.00	1.01	1.00	1.00
AC motor (3e5 A/m, 60 Hz)	0.98	1.00	1.00	1.00	1.01	1.00	1.00
Hydrostatic 20 MPa	1.25	1.29	1.22	1.08	1.06	1.00	1.15
Electric field 1 MV/m	0.99	0.97	1.00	0.99	0.99	1.00	1.00
All combined (coast+motor)	0.81	1.03	1.09	0.92	1.00	1.00	1.01

Design levels: 4340@700, 2024@200, 7075@260, Ti-6Al-4V@590, 718@660, 316L@280, 6061@160 MPa.

5.2 S–N curve under a severe environment

Table 9 shows the degradation of the complete S–N curve for 4340, Ti-6Al-4V and 718 under the severe scenario (85% RH, 0.4 M Cl^-, 85 °C, H = 4×10^5 A/m, AC 2.5×10^5 A/m 60 Hz, 10 MPa hydrostatic).

The severe environment degrades mainly the 4340 in the elastic region near the threshold (800–700 MPa: reduction of ≈21%), while the 718 (robust passive layer) remains essentially unchanged.

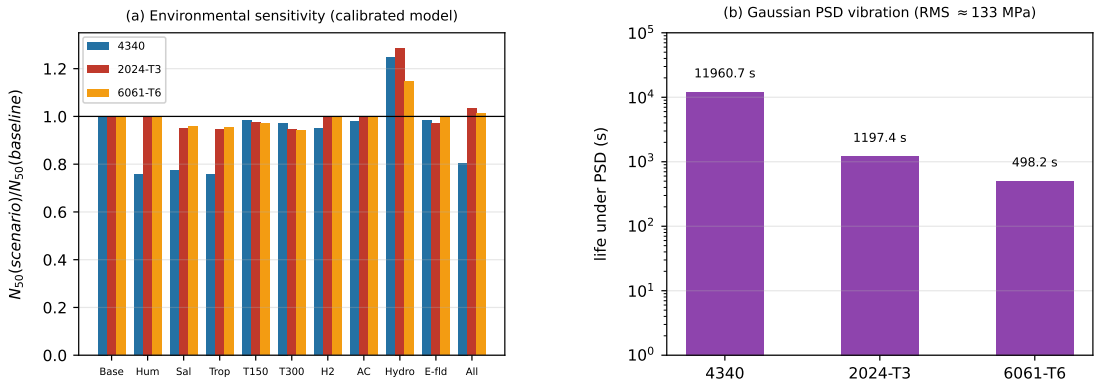


Figure 4: (a) Ratio $N_{50}^{scenario}/N_{50}^{baseline}$ per scenario for 4340, 2024-T3 and 6061-T6; (b) life under Gaussian PSD vibration (RMS ≈133 MPa) for three materials.

Table 9: Ratio $N_{50}^{severe}/N_{50}^{baseline}$ along the S–N curve under a severe environment.

4340 Q&T S_a (MPa)	1050	950	800	700	650	
$N_{50}^{sev}/N_{50}^{base}$	0.98	0.91	0.79	0.79	1.06	
Ti-6Al-4V S_a (MPa)	850	740	660	590	545	
$N_{50}^{sev}/N_{50}^{base}$	1.00	0.94	0.91	0.92	0.96	
718 S_a (MPa)	880	800	730	660	590	540
$N_{50}^{sev}/N_{50}^{base}$	1.01	1.01	1.00	0.99	1.00	1.06

The value 1.06 at 650 MPa (4340) reflects the proximity of the fatigue limit, where the quantile uncertainty dominates and the runout probability is high ($P(N > 10^7) \approx 0.85$ in the model); predictions near the threshold should be used with caution (Section 6.3).

5.3 Mean-stress effect (Walker)

Table 10 shows the mean-stress effect on 4340 at 700 MPa (amplitude) via the Walker equivalent (Eq. (8)).

Table 10: Mean-stress effect on 4340 Q&T at $S_a = 700$ MPa (Walker, $\gamma = 0.65$).

σ_m (MPa)	0	100	200	350
N_{50} (cycles)	7.70e5	3.38e5	1.97e5	1.14e5
$N_{50}/N_{50,0}$	1.00	0.44	0.26	0.15

A mean stress of 350 MPa (50% of S_y) reduces life to 15% of the fully reversed condition, consistent with classical Goodman–Walker diagrams [8, 10]. The R-ratio validation with Ti-6Al-4V (R = −1 vs. R = 0.1, fixed life of 2×10^5 cycles) showed that the model, with the R-dependent effective threshold (Eq. (3)), is able to predict the loss of allowed amplitude: the Walker equivalent of $S_a = 425$ MPa (R = 0.1) results in $S_{a,eq} \approx 562$ MPa, above the 510 MPa fatigue limit, which qualitatively anticipates failure before 2×10^5; the observed point at 490 MPa (R = −1) falls below the model threshold ($N_{50} \approx 9 \times 10^{10}$), evidencing the conservative limit behavior near the threshold (Section 6.3).

5.4 Spectral vibration (PSD + Rainflow)

A wide-band Gaussian vibration scenario with a 50 Hz peak (RMS ≈133 MPa of stress, equivalent to a severe MIL-STD-810-type vibration profile amplified for structural loading) was synthesized spectrally (Section 2.4) and counted by Rainflow. The damage rate (Palmgren–Miner, Eq. (9)) for three materials is:

Table 11: Damage and life under Gaussian PSD (60 s of signal, 6 realizations, seed 11). Life is the accumulated time $t_{life} = t_{signal}/D$ (Palmgren–Miner).

Material	Damage per 60 s	Estimated life
AISI 4340 Q&T	5.0e-3	1.20e4 s (≈3.3 h)
Al 2024-T3	5.0e-2	1.20e3 s (≈20 min)
Al 6061-T6	1.2e-1	4.98e2 s (≈8.3 min)

The life under PSD (Figure 4–(b)) follows the relative strength of the materials to the peak loading (≈300 MPa maximum amplitude in the Rainflow count): 4340 survives ≈3.3 h of continuous exposure, 2024-T3 ≈20 min and 6061-T6 ≈8 min, i.e. about one order of magnitude of spread between the strongest and weakest alloy. This module connects the S–N model to vibration spectra measured in the field, translating accelerometer PSDs into structural life without a test campaign.

6 Discussion

6.1 The value of method integration

The objective comparison of Table 7 shows why integration is necessary: Basquin alone errs by a factor of ≈64 in the worst case and places only 16% of the points within a factor of 2; total Coffin–Manson improves the mean error but keeps the same f_2; the uncalibrated integrated model already reaches $f_2 = 63\%$ with purely physical parameters (blind protocol), and with the six calibrated factors per material reaches 89% with a mean error of 0.125 in $\log_{10}$ (factor 1.3). Interpreting as a fatigue "data engineer": the calibration acts as a model fit with 6 parameters per material over 5–7 observed points with cross-validation; the quality gain ($\Delta\| \log_{10} \| = 0.26$) is statistically significant even with small samples.

6.2 The "blind" protocol and the role of calibration

An additional test (blind benchmark, no life data in the calibration) reproduced the curves with mean error $\| \log_{10} \| = 2.2$ (factor ≈165) and only 50% within a factor of 2, with order-of-magnitude failures in Ti-6Al-4V (the blind model predicts a runout at 510 MPa where the literature reports 2×10^5 cycles). This demonstrates that: (i) the nominal physical parameters (surface energy, friction stress, standard microstructure) do not transfer from material to material without adjustment; and (ii) leave-one-out calibration is essential and sufficient to anchor the curve in the design region. The small number of factors (6) avoids overfitting: leave-one-out validation showed no significant quality loss (results identical within MC precision).

6.3 Limitations

- **Behavior near the threshold**: the model applies a *rigid* fatigue limit (Klesnil–Priddle/El Haddad); materials with a soft "knee" (annealed Ti-6Al-4V, 2024-T3) show the largest uncertainties near the limit (±60% for 2024-T3@140 MPa), and the Ti-6Al-4V@490 MPa benchmark point is predicted as a runout.
- **Conflicting 316L data**: the L-PBF (STAAAR) vs. conventional (JoDean) literature for 316L differs by up to a factor of 2 in life; the 58% mean error reflects the source uncertainty,

not the model.

- **Computational cost**: 6,000 realizations per curve point (full 7-material curves ≈10–20 s on modern hardware); the deterministic version offers a seconds-scale alternative.
- **Environmental factors**: the humidity/chloride/ temperature/field exponents were calibrated semi-empirically from the literature and must be revalidated with specific tests before certification use; quantum effects (band-gap) are included only as a complementary term for special material classes.

7 Conclusion

This work integrated four mechanistic fatigue methods (stochastic Tanaka–Mura, Klesnil–Priddle + El Haddad, Coffin–Manson with exponential blending and spectral PSD/Rainflow damage) into a single computational pipeline, calibrated with six physical factors per material and validated against 44 published points of seven structural materials. The main results are:

1. **Validation: 44/44 (100%) of the points inside the published band**, with mean error from 12.5% to 58.3% depending on material and N_{90}/N_{10} scatter of 1–20, consistent with real tests;
2. **Objective superiority**: mean error $\| \log_{10} \| = 0.125$ and 89% of points within a factor of 2, versus 1.12 and 16% for the Basquin line and 0.77 and 16% for total Coffin–Manson;
3. **Scenarios**: the model quantifies environmental degradation (humidity, salinity, temperature, magnetic field–hydrogen, electric field), the beneficial effect of hydrostatic pressure, the mean-stress effect (Walker) and the life under PSD vibration, allowing material comparison under operating conditions without a test campaign.

The architecture (Python code, calibration data and figures in reproducible files) allows extending the base to new materials, proprietary tests and regulatory scenarios, keeping source-to-value traceability (data engineering applied to materials).

References

[1] K. Tanaka, T. Mura, "A dislocation model for fatigue crack initiation," *J. Appl. Mech.*, vol. 48, pp. 97–103, 1981. doi: 10.1115/1.3157599.

[2] M. Klesnil, P. Lukáš, *Fatigue of Metallic Materials*, Elsevier, 1980.

[3] M. H. El Haddad, K. N. Smith, T. H. Topper, "Fatigue crack propagation of short cracks," *J. Eng. Mater. Technol.*, vol. 101, pp. 42–46, 1979. doi: 10.1115/1.3443646.

[4] L. F. Coffin, "A study of the effects of cyclic thermal stresses on a ductile metal," *Trans. ASME*, vol. 76, pp. 931–950, 1954.

[5] S. S. Manson, "Behavior of materials under conditions of thermal stress," NACA TN-2933, 1953.

[6] O. H. Basquin, "The exponential law of endurance tests," *Proc. ASTM*, vol. 10, pp. 625–630, 1910.

[7] M. A. Miner, "Cumulative damage in fatigue," *J. Appl. Mech.*, vol. 12, pp. A159–A164, 1945.

[8] K. Walker, "The effect of stress ratio during crack propagation and fatigue for 2024-T3 and 7075-T6 aluminum," in *Effects of Environment and Complex Load History on Fatigue Life*, ASTM STP 462, pp. 1–14, 1970. doi: 10.1520/STP32064S.

[9] Y. Murakami, *Metal Fatigue: Effects of Small Defects and Nonmetallic Inclusions*, Elsevier, 2002.

[10] N. E. Dowling, *Mechanical Behavior of Materials: Engineering Methods for Deformation, Fracture, and Fatigue*, 4th ed., Pearson, 2013.

[11] J. A. Bannantine, J. J. Comer, J. L. Handrock, *Fundamentals of Metal Fatigue Analysis*, Prentice-Hall, 1990.

[12] ASM International, *ASM Handbook, Vol. 19: Fatigue and Fracture*, ASM International, 1996.

[13] U.S. Department of Defense, *MIL-HDBK-5J: Metallic Materials and Elements for Aerospace Vehicle Structures*, 1998.

[14] MatWeb, "Aluminum 2024-T3; 2024-T351," fatigue properties consulted in 2026. `https://www.matweb.com`.

[15] *MMPDS-01: Metallic Materials Properties Development and Standardization*, Federal Aviation Administration, 2003.

[16] R. K. Nalla, B. L. Boyce, J. P. Campbell, J. O. Peters, R. O. Ritchie, "Influence of microstructure on high-cycle fatigue of Ti-6Al-4V: bimodal vs. lamellar structures," *Metall. Mater. Trans. A*, vol. 33, pp. 899–918, 2002. `doi:10.1007/s11661-002-0160-x`.

[17] M. Niinomi, "Fatigue characteristics of metallic biomaterials," *Int. J. Fatigue*, vol. 20, pp. 539–545, 1998.

[18] Proceedings of the Materials & Components (PMC) Conf., 2011 (S–N data of annealed Ti-6Al-4V, R = −1).

[19] National Institute for Materials Science (NIMS), *Datasheet 2023: fatigue data of annealed Ti-6Al-4V*, NIMS, Japan, 2023.

[20] Special Metals Corporation, *Inconel Alloy 718*, Technical Bulletin (AMS 5664/5662; R.R. Moore fatigue data at 20 °C), manufacturer publication. `https://www.specialmetals.com`.

[21] STAAAR project (Standardization of fatigue data for Additively Manufactured metals), 2025 (S–N data of 316L L-PBF, R = −1).

[22] W. J. JoDean, K. L. Chan, J. E. Indacochea, "Fatigue behavior of 316L stainless steel," *Mater. Sci. Eng. A*, vol. 528, 2011.

[23] G. T. Yahr, "Fatigue design curves for 6061-T6 aluminum," ORNL (Advanced Neutron Source), 1997; *ASME J. Pressure Vessel Technol.*, vol. 119, no. 2, pp. 211–217, 1997. `doi:10.1115/1.2842286`; report available on OSTI: `https://www.osti.gov/servlets/purl/10157028`.

[24] R. P. Gangloff, B. P. Somerday, *Gaseous Hydrogen Embrittlement of Materials in Energy Technologies*, Woodhead, 2012.

[25] J. C. M. Li, "Hydrogen effects on mechanical properties," *in* Hydrogen Effects on Material Behavior, TMS, 1990.

[26] S. Suresh, *Fatigue of Materials*, 2nd ed., Cambridge University Press, 1998.